J. Fluid Mech. (2007), *vol.* 582, *pp.* 53–78.
doi:10.1017/S0022112007005691 Printed in the United Kingdom

Linear stability of the flow past a spheroidal bubble

BINZE YANG[1] AND ANDREA PROSPERETTI[1,2]†

[1]Department of Mechanical Engineering, The Johns Hopkins University, Baltimore, MD 21218, USA
[2]Faculty of Applied Science and Burgerscentrum, University of Twente, AE 7500 Enschede, The Netherlands

(Received 31 December 2005 and in revised form 3 January 2007)

The linear stability of the axisymmetric flow past a fixed-shape spheroid with free-slip boundary conditions is studied numerically to gain some insight into the path instability of bubbles rising in liquids. Qualitatively, the results are similar to those for a solid sphere. The $m = 1$ mode gives rise to a double-threaded wake and proves to be the most unstable mode, with a first regular bifurcation followed by a Hopf bifurcation. The importance of the base-flow vorticity is highlighted by a stability analysis of the axisymmetric base flow 'frozen' before reaching steady state. Setting viscosity to zero in the perturbation equations results in a faster growth of the primary instability, which indicates its root in inertial effects.

1. Introduction

A millimetre-diameter gas bubble rising in still water is often observed to follow a zigzag or spiral path (see e.g. Clift, Grace & Weber 1978; Magnaudet & Eames 2000). This phenomenon, referred to as path instability or 'Leonardo's paradox' (Prosperetti 2004) in the literature, has attracted considerable attention in the last 50 years.

Saffman (1956) reported the onset of path instability at an equivalent radius $R_{eq} = 0.7$ mm: a straight path for $R_{eq} \leqslant 0.7$ mm, a zigzag for $0.7 \leqslant R_{eq} \leqslant 1.0$ mm, and both zigzag and spiral for $R_{eq} \geqslant 1.0$ mm. The corresponding critical Reynolds number defined in terms of the bubble equivalent diameter, terminal velocity and liquid kinematic viscosity, was estimated to be $Re_c \simeq 400$. Hartunian & Sears (1957) estimated a critical Reynolds number of $Re_c = 202$, similar to that for the flow past a solid sphere; the corresponding bubble radius was 0.63 mm. Aybers & Tapucu (1969*a*, *b*) found a rectilinear path for $R_{eq} \leqslant 0.67$ mm, spiral for $0.67 \leqslant R_{eq} \leqslant 1$ mm, zigzag changing into spiral for $1 \leqslant R_{eq} \leqslant 1.8$ mm, and zigzag for $1.8 \leqslant R_{eq} \leqslant 2.1$ mm. In an experimental study, Shew, Poncet & Pinton (2006) estimate a critical Reynolds number around 720.

It is now believed that the numerical inconsistency among these results is related to the purity of the water used in the experiments and, more specifically, to the presence of surface-active substances. For a long time it was thought that such impurities affected the results not only quantitatively, but also qualitatively. The experiments of Duineveld (1995) with hyper-clean water, however, proved the latter belief to be incorrect. While he found the onset of zigzagging at $R_{eq} = 0.91$ mm and $Re_c = 662$, the basic qualitative features of the phenomenon and its dependence on

† Author to whom correspondence should be addressed: prosperetti@jhu.edu.

bubble radius were confirmed. A similar conclusion was reported by Lunde & Perkins (1998) and Ellingsen & Risso (2001) who studied the path instability of bubbles with $R_{eq} \simeq 1.2\,\mathrm{mm}$, and by de Vries, Biesheuvel & van Wijngarden (2002) in purified water.

The focus on the precise nature of the boundary condition at the bubble surface and the presumed difference between clean and contaminated water led workers to believe that the physics of the instability was different from that observed with solid objects, such as spheres. For a relatively large Reynolds number and a free-slip surface, most of the flow field is irrotational except for a thin wake behind the bubble. Therefore, Hartunian & Sears (1957), el Sawi (1974) and Benjamin (1987) analysed path instability using the irrotational flow assumption. However, the predicted non-zero drift angle from irrotational theory was not observed in experiments. By considering the growth of linear three-dimensional perturbations, Meiron (1989) concluded that no instability occurs in potential flow, which shows that the vortical wake must play an essential role. This result supported the conjecture of Saffman (1956), who was the first to hypothesize a coupling between the path and wake instabilities.

Another feature of bubbles as opposed to solid objects debated in the literature is deformability and possible shape oscillations. On the basis of inviscid theory, el Sawi (1974) found that, beyond a Weber number of about 3.3, no steady solution was possible. From the proximity of this value to that reported by Hartunian & Sears (1957) for the onset of path instability, he hypothesized a possible role of shape oscillations. Duineveld (1995) (see also Magnaudet & Eames 2000) disproved this notion, although shape oscillations do exist for larger bubbles as shown by Lunde & Perkins (1998).

Progress in the understanding of the wake behind solid spheres, on the one hand, and behind a rising bubble, on the other, gradually brought to light the existence of substantial similarities between the two situations in spite of the different mechanism of surface vorticity generation (see e.g. Batchelor 1967; Leal 1989).

Natarajan & Acrivos (1993) carried out a linear stability analysis of the steady axisymmetric flow past a fixed sphere and found a first loss of stability via a regular bifurcation to a steady flow at $Re \simeq 210$. This flow is characterized by the existence of a plane of symmetry and by a two-threaded wake consisting of streamwise vorticity of opposite signs. The existence of this wake, first observed by Magarvey & Bishop (1961), is sufficient to explain the onset of a 'lift' force at right angles to the incoming steady flow. With increasing Reynolds number, Natarajan & Acrivos found a second eigenvalue becoming unstable via a Hopf bifurcation at $Re = 277.5$. A similar sequence was found in the fully nonlinear three-dimensional calculations of Johnson & Patel (1999), Tomboulides & Orszag (2000) and Ghidersa & Dušek (2000). The latter authors argued that, for Reynolds numbers not too far above the second bifurcation point, the essential physics of the process is captured by the first two unstable modes. This basic picture of wake transition was confirmed in the further calculations of Thompson, Leweke & Provansal (2001) and in the experiments of Ormières & Provansal (1999), Schouveiler & Provansal (2002), Jenny, Dušek & Bouchet (2004), and Veldhuis *et al.* (2005).

A parallel experimental effort on rising bubbles revealed a similar pattern. Lunde & Perkins (1997) and Brücker (1999) found the typical two-threaded wake and strong qualitative similarities with solid spheres. The study of de Vries *et al.* (2002) in highly purified water proved that these results were robust and not affected by water quality. Direct numerical simulations of axisymmetric flow confirmed the existence of a steady attached eddy behind a rectilinearly rising bubble with both a fixed (see Blanco &

Magnaudet 1995; Takagi, Matsumoto & Huang 1997) and a free (see Ryskin & Leal 1984) shape in a certain range of Reynolds numbers. The simulations of the free rise of a fixed-shape spheroid with free-slip boundary conditions by Mougin & Magnaudet (2002) exhibited the same qualitative and quantitative features of a real bubble (Ellingsen & Risso 2001): an initially rectilinear rise, followed by a bending of the trajectory, the onset of zigzag, and eventually a spiral path. The presence of a two-threaded wake was also unmistakable.

Although the work carried out to date has shed a significant light on the mechanics of path instability, the root physical cause of this intriguing phenomenon has not been revealed. In the present paper, we carry out a linear stability study of the axisymmetric flow past a free-slip spheroid with a fixed shape, as assumed by Magnaudet & Mougin (2007). This approach enables us to investigate the role of several features of the flow (vorticity distribution in the wake, vorticity of the perturbation) which cannot be analysed in a fully three-dimensional study.

The relevance of the stability properties of a fixed body *vs.* those of a body free to move is somewhat unclear. Both Magnaudet & Mougin (2007) and we find that the first instability is supercritical for a fixed spheroid.† On the other hand, as noted by Goldburg & Florsheim (1966), some quantitative features such as the Strouhal number of the flow past a solid body seem not to be much affected by the constraint. Furthermore, qualitative features of the wake, such as the presence of hairpin vortices, appear to be remarkably robust as revealed, for example, by a comparison of the data of Achenbach (1974) and Schouveiler & Provansal (2002) with, for example, those of Veldhuis *et al.* (2005).

2. Problem statement

We study the flow past a stationary spheroidal bubble with a prescribed fixed shape and free-slip boundary conditions.

We write the velocity and pressure fields as $\boldsymbol{U}+\boldsymbol{u}$, $P+p$, where $\boldsymbol{U}$, P are the fields of the base axisymmetric flow and $\boldsymbol{u}$, p the perturbation. The base flow is governed by the standard Navier–Stokes equations which we write in non-dimensional form as

$$\frac{\partial \boldsymbol{U}}{\partial t}+\boldsymbol{\nabla}\cdot(\boldsymbol{U}\boldsymbol{U})+\boldsymbol{\nabla}P+2Re^{-1}\boldsymbol{\nabla}\times(\boldsymbol{\nabla}\times\boldsymbol{U})=0, \quad \boldsymbol{\nabla}\cdot\boldsymbol{U}=0. \tag{2.1}$$

The non-dimensionalization is in terms of the equivalent spherical radius of the bubble, R_{eq}, and the (constant) velocity of the incident flow U_∞, so that the Reynolds number is defined as $Re=2R_{eq}U_\infty/\nu$, with ν the kinematic viscosity of the liquid. The perturbation fields satisfy the linearized form of the Navier–Stokes equations:

$$\frac{\partial \boldsymbol{u}}{\partial t}+\boldsymbol{\nabla}\cdot(\boldsymbol{U}\boldsymbol{u}+\boldsymbol{u}\boldsymbol{U})+\boldsymbol{\nabla}p+2Re^{-1}\boldsymbol{\nabla}\times(\boldsymbol{\nabla}\times\boldsymbol{u})=0, \quad \boldsymbol{\nabla}\cdot\boldsymbol{u}=0. \tag{2.2}$$

At the bubble surface we impose the kinematic condition of vanishing normal velocity and the dynamic condition of vanishing tangential stress. The normal stress condition cannot be satisfied owing to the adoption of a prescribed fixed shape. The calculation is initialized by placing the bubble in a uniform incident flow.

† In an earlier paper, Mougin & Magnaudet (2002) mentioned the possibility of a subcritical bifurcation for a free spheroid; Professor Magnaudet has kindly informed us that a more recent analysis of those data suggests that the bifurcation remains supercitical.

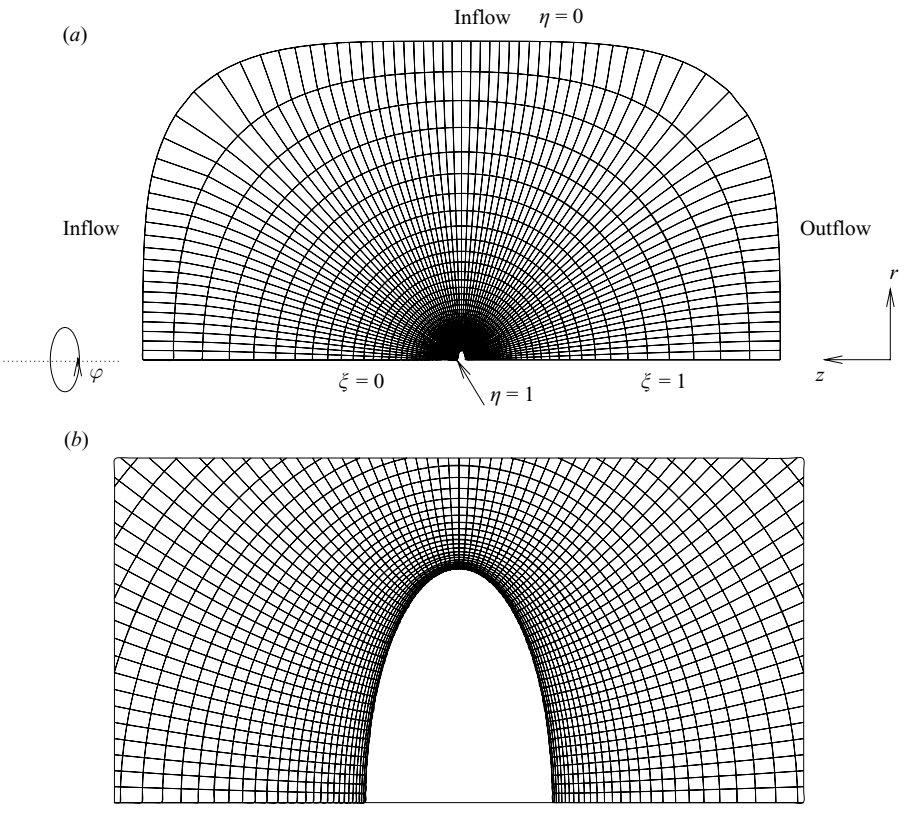

FIGURE 1. The computational domain and boundary-fitted grid. (*a*) Overview. (*b*) Detail.

2.1. *Base flow*

Following Dandy & Leal (1986) and Blanco & Magnaudet (1995), in the meridian plane, we use boundary fitted coordinates (ξ, η) generated as described in the next section. The coordinate ξ varies in the direction parallel to the bubble surface, while η is normal to it (see figure 1). The bubble surface corresponds to $\eta = 1$, the outer boundary to $\eta = 0$, the part of the symmetry axis ahead of the bubble to $\xi = 0$, and the part downstream to $\xi = 1$.

In these coordinates, the continuity equation for the base flow is

$$\frac{1}{h_\xi h_\eta r}\left[\frac{\partial}{\partial \xi}(h_\eta r U_\xi) + \frac{\partial}{\partial \eta}(h_\xi r U_\eta)\right] = 0, \tag{2.3a}$$

where r is the distance from the symmetry axis, h_ξ, h_η are the scale factors in the ξ- and η-direction, and $\boldsymbol{U} = (U_\xi, U_\eta)$. The momentum equations are

$$\begin{aligned}\frac{\partial U_\xi}{\partial t} + \frac{1}{h_\xi h_\eta r}\left[\frac{\partial}{\partial \xi}\left(h_\eta r U_\xi^2\right) + \frac{\partial}{\partial \eta}(h_\xi r U_\xi U_\eta) + r U_\eta\left(U_\xi \frac{\partial h_\xi}{\partial \eta} - U_\eta \frac{\partial h_\eta}{\partial \xi}\right)\right] \\ = \frac{2Re^{-1}}{h_\eta r}\left\{\frac{\partial}{\partial \eta}\left[\frac{r}{h_\xi h_\eta}\frac{\partial}{\partial \eta}(h_\xi u_\xi)\right] - \frac{\partial}{\partial \eta}\left[\frac{r}{h_\xi h_\eta}\frac{\partial}{\partial \xi}(h_\eta u_\eta)\right]\right\} - \frac{1}{h_\xi}\frac{\partial P}{\partial \xi},\end{aligned} \tag{2.3b}$$

$$\frac{\partial U_\eta}{\partial t}+\frac{1}{h_\xi h_\eta r}\left[\frac{\partial}{\partial\xi}(h_\eta r U_\xi U_\eta)+\frac{\partial}{\partial\eta}\left(h_\xi r U_\eta^2\right)+rU_\xi\left(U_\eta\frac{\partial h_\eta}{\partial\xi}-U_\xi\frac{\partial h_\xi}{\partial\eta}\right)\right]$$
$$=\frac{2Re^{-1}}{h_\xi r}\left\{\frac{\partial}{\partial\xi}\left[\frac{r}{h_\xi h_\eta}\frac{\partial}{\partial\xi}(h_\eta U_\eta)\right]-\frac{\partial}{\partial\xi}\left[\frac{r}{h_\xi h_\eta}\frac{\partial}{\partial\eta}(h_\xi U_\xi)\right]\right\}-\frac{1}{h_\eta}\frac{\partial P}{\partial\eta}. \quad (2.3c)$$

The zero tangential stress condition at the bubble surface $\eta=1$ is

$$\frac{h_\xi}{h_\eta}\frac{\partial}{\partial\eta}\left(\frac{U_\xi}{h_\xi}\right)+\frac{h_\eta}{h_\xi}\frac{\partial}{\partial\xi}\left(\frac{U_\eta}{h_\eta}\right)=0, \quad (2.4)$$

while the zero normal velocity condition is $U_\eta=0$. On the symmetry axes $\xi=0$ and $\xi=1$, the natural conditions are

$$U_\xi=0, \qquad \frac{\partial U_\eta}{\partial\xi}=0. \quad (2.5)$$

2.2. *Perturbation*

We expand the perturbation fields $\boldsymbol{u}$, p in a Fourier series in the angular coordinate φ around the axis of symmetry of the base flow as

$$\boldsymbol{u}=\sum_{-\infty}^{\infty}\boldsymbol{u}^m(\xi,\eta,t)\mathrm{e}^{\mathrm{i}m\varphi}, \qquad p=\sum_{-\infty}^{\infty}p^m(\xi,\eta,t)\mathrm{e}^{\mathrm{i}m\varphi}. \quad (2.6)$$

Since $\boldsymbol{u}$ and p are real-valued physical quantities, $\boldsymbol{u}^{-m}=\overline{\boldsymbol{u}^m}$ and $p^{-m}=\overline{p^m}$, where the overbar denotes the complex conjugate. Upon substitution of (2.6) into (2.2) and separation of the angular modes, the linearized equations in (ξ,η,φ) coordinates become

$$\frac{\partial(h_\eta r u_\xi)}{\partial\xi}+\frac{\partial(h_\xi r u_\eta)}{\partial\eta}+mh_\xi h_\eta u_\varphi=0, \quad (2.7a)$$

$$\frac{\partial u_\xi}{\partial t}+\frac{1}{h_\xi h_\eta r}\left\{2\frac{\partial(h_\eta r U_\xi u_\xi)}{\partial\xi}+\frac{\partial}{\partial\eta}[h_\xi r(U_\eta u_\xi+U_\xi u_\eta)]\right.$$
$$\left.+r\frac{\partial h_\xi}{\partial\eta}(U_\eta u_\xi+U_\xi u_\eta)-2rU_\eta u_\eta\frac{\partial h_\eta}{\partial\xi}+mh_\xi h_\eta U_\xi u_\varphi\right\}$$
$$=\frac{2Re^{-1}}{h_\eta r}\left\{\frac{\partial}{\partial\eta}\left[\frac{r}{h_\xi h_\eta}\frac{\partial(h_\xi u_\xi)}{\partial\eta}\right]-\frac{\partial}{\partial\eta}\left[\frac{r}{h_\xi h_\eta}\frac{\partial(h_\eta u_\eta)}{\partial\xi}\right]-\frac{m^2h_\eta u_\xi}{r}-\frac{mh_\eta}{h_\xi r}\frac{\partial(ru_\varphi)}{\partial\xi}\right\}-\frac{1}{h_\xi}\frac{\partial p}{\partial\xi}, \quad (2.7b)$$

$$\frac{\partial u_\eta}{\partial t}+\frac{1}{h_\xi h_\eta r}\left\{\frac{\partial}{\partial\xi}[h_\eta r(U_\eta u_\xi+U_\xi u_\eta)]+2\frac{\partial(h_\xi r U_\eta u_\eta)}{\partial\eta}\right.$$
$$\left.+r\frac{\partial h_\eta}{\partial\xi}(U_\eta u_\xi+U_\xi u_\eta)-2rU_\xi u_\xi\frac{\partial h_\xi}{\partial\eta}+mh_\xi h_\eta U_\eta u_\varphi\right\}$$
$$=\frac{2Re^{-1}}{h_\xi r}\left\{\frac{\partial}{\partial\xi}\left[\frac{r}{h_\xi h_\eta}\frac{\partial(h_\eta u_\eta)}{\partial\xi}\right]-\frac{\partial}{\partial\xi}\left[\frac{r}{h_\xi h_\eta}\frac{\partial(h_\xi u_\xi)}{\partial\eta}\right]-\frac{m^2h_\xi u_\eta}{r}-\frac{mh_\xi}{rh_\eta}\frac{\partial(ru_\varphi)}{\partial\eta}\right\}-\frac{1}{h_\eta}\frac{\partial p}{\partial\eta}, \quad (2.7c)$$

$$\frac{\partial u_\varphi}{\partial t} = -\frac{1}{h_\xi h_\eta r}\left[\left(U_\xi h_\eta \frac{\partial r}{\partial \xi} + U_\eta h_\xi \frac{\partial r}{\partial \eta}\right) u_\varphi + \frac{\partial (h_\eta r U_\xi u_\varphi)}{\partial \xi} + \frac{\partial (h_\xi r U_\eta u_\varphi)}{\partial \eta}\right] + \frac{2Re^{-1}}{h_\xi h_\eta}\left\{m\frac{\partial}{\partial \xi}\left(\frac{h_\eta u_\xi}{r}\right) + m\frac{\partial}{\partial \eta}\left(\frac{h_\xi u_\eta}{r}\right) + \frac{\partial}{\partial \xi}\left[\frac{h_\eta}{r h_\xi}\frac{\partial (r u_\varphi)}{\partial \xi}\right] + \frac{\partial}{\partial \eta}\left[\frac{h_\xi}{r h_\eta}\frac{\partial (r u_\varphi)}{\partial \eta}\right]\right\} + \frac{m}{r}\, p, \tag{2.7d}$$

where iu_φ has been replaced by u_φ. Since, owing to the linearization, different values of m are not coupled, we have dropped the superscript m for simplicity.

As before, the kinematic boundary condition at the bubble surface $\eta = 1$ is simply $u_\eta = 0$. The tangential stress condition now gives rise to the two relations:

$$\frac{h_\xi}{h_\eta}\frac{\partial}{\partial \eta}\left(\frac{u_\xi}{h_\xi}\right) + \frac{h_\eta}{h_\xi}\frac{\partial}{\partial \xi}\left(\frac{u_\eta}{h_\eta}\right) = 0, \tag{2.8a}$$

$$\frac{1}{h_\eta}\frac{\partial u_\varphi}{\partial \eta} - \frac{m u_\eta}{r} - \frac{u_\varphi}{h_\eta r}\frac{\partial r}{\partial \eta} = 0. \tag{2.8b}$$

In order to treat properly the singularity on the axis of symmetry, we demand that

$$u_\xi = 0, \quad u_\varphi = 0, \quad \frac{\partial u_\eta}{\partial \xi} = 0, \quad \frac{\partial p}{\partial \xi} = 0, \qquad m \text{ even},$$

$$\frac{\partial u_\xi}{\partial \xi} = 0, \quad \frac{\partial u_\varphi}{\partial \xi} = 0, \quad u_\eta = 0, \quad p = 0, \qquad m \text{ odd}.$$

3. Numerical formulation

The computational domain (figure 1*a*) is bounded by the bubble surface, the symmetry axis, and an outer boundary given as a Lamé curve $(r/r_1)^n + (z/z_1)^n = 1$, where r and z are cylindrical coordinates defined in the usual way, with z oriented toward the incoming flow and r_1 and z_1 constants. The bubble is approximated as a spheroid with a fixed shape and aspect ratio $\chi = b/a$, with a and b the minor and major semi-axes, respectively. A similar model has been introduced by Moore (1965) and used by Blanco & Magnaudet (1995), Mougin & Magnaudet (2002) and Magnaudet & Mougin (2007). The experimental data of Duineveld (1995) support the approximation.

The computations are carried out on an orthogonal boundary-fitted grid (ξ, η) generated by the technique of Duraiswami & Prosperetti (1992), which belongs to the family of orthogonal mappings proposed by Ryskin & Leal (1983) and already used, for example, in Blanco & Magnaudet (1995), Takagi *et al.* (1997), and Yang, Prosperetti & Takagi (2003). Figure 1(*a*) is an example of the numerical grid, and figure 1(*b*) shows a detail of the grid near the bubble surface.

The boundary conditions on the bubble surface and the symmetry axis were specified in the previous section. For the base flow, on the outer boundary $\eta = 0$, we prescribe the undisturbed velocity outside the wake and outflow conditions in the neighbourhood of the wake. Specifically, we impose

$$\text{inflow } U_\xi = \frac{1}{h_\xi}\frac{\partial z}{\partial \xi}, \quad U_\eta = \frac{1}{h_\eta}\frac{\partial z}{\partial \eta}, \qquad 1 \geqslant N_z \geqslant -\frac{1}{\sqrt{2}},$$

$$\text{outflow } \frac{\partial U_\xi}{\partial \eta} = 0, \quad \frac{\partial^2 U_\eta}{\partial^2 \eta} = 0, \qquad -\frac{1}{\sqrt{2}} \geqslant N_z \geqslant -1,$$

where N_z is the z-component of the outward unit normal to the computatonal boundary. The outflow condition stipulates zero normal derivative for the tangential velocity, $(\boldsymbol{N}\cdot\nabla)U_\xi = 0$, with the parabolic approximation on the normal velocity advocated by Magnaudet, Rivero & Fabre (1995). We also experimented with zero tangential stress and zero normal velocity conditions in the region $-1/\sqrt{2} < N_z < 1/\sqrt{2}$ which proved suitable but required a much finer grid near the boundary.

For the perturbation we used similar conditions, with a zero perturbation velocity in the range $1 \geqslant N_z \geqslant -1/\sqrt{2}$ and the parabolic conditions on the remainder of the boundary augmented by $\partial u_\varphi/\partial\eta = 0$.

3.1. *Algorithm*

Equations (2.3*a–c*), with the corresponding boundary conditions, are solved by finite differences on a staggered grid. We use a pressure-increment projection method with a semi-implicit discretization for the nonlinear terms (see Brown, Cortez & Minion 2001) which we have adapted to the present case of free-slip boundary conditions (Yang & Prosperetti 2006). The standard Neumann conditions for the auxiliary pressure variable are imposed on all the boundaries. The method has second-order accuracy in space and time.

The perturbation equations (2.7*a–d*) are integrated in time with the same numerical algorithm. It is important to use the conservative form of the equations, and the discretization should be consistent with that used for the computation of the base flow. By replacing u_φ by $\mathrm{i}u_\varphi$ it is possible to deal exclusively with real quantities.

For all the cases with $Re = 660$ we used the same constant (non-dimensional) time step 0.012, which always satisfied the CFL stability constraint based on the instantaneous maximum velocity. For each of the other cases, the time step was also kept fixed for the entire simulation and adjusted to satisfy the CFL condition.

3.2. *Initial conditions*

The solution for the base flow is calculated starting from a uniform flow. The correct boundary conditions develop automatically by the end of the first time step.

For the purposes of a stability analysis, one should make sure that the initial conditions imposed on the perturbation contain the most unstable mode of the linear system. Since there is no systematic way of achieving this objective, we have experimented with two different classes of initial conditions. The first class consists of $u_\varphi = 0$, while u_η is given by

$$u_\eta = \begin{cases} \cos(2k_1\pi\xi)\sin(2k_2\pi\eta), & m \text{ even}, \\ \sin(2k_1\pi\xi)\sin(2k_2\pi\eta), & m \text{ odd}, \end{cases} \tag{3.1}$$

with u_ξ calculated from the incompressibility constraint (2.7*a*). The second class uses (3.1) for u_η, but replaces $u_\varphi = 0$ with

$$u_\varphi = \begin{cases} \sin(2k_1\pi\xi)\sin(2k_2\pi\eta), & m \text{ even}, \\ \cos(2k_1\pi\xi)\sin(2k_2\pi\eta), & m \text{ odd}. \end{cases} \tag{3.2}$$

In these expressions, k_1 and k_2 are arbitrary non-negative integers. For both classes, u_ξ, u_η and u_φ vanish at the outer boundary and at the bubble surface.

We tested various combinations of the integers k_1 and k_2 in (3.1) and (3.2). The results show that, after a short initial transient, the evolution of the perturbation is insensitive to both the type of the initial perturbation and the specific values of k_1 and k_2; the results shown below have been obtained with $k_1 = k_2 = 1$ and $u_\varphi = 0$.

	Present	Other investigators
$Re = 200$, $\chi = 1.0$	0.203	0.200
$Re = 600$, $\chi = 1.0$	0.072	0.072
$Re = 664$, $\chi = 1.75$	0.104	0.102
$Re = 660$, $\chi = 2.0$	0.126	0.120
$Re = 200$, Solid sphere	0.79	0.79/0.78

TABLE 1. Comparison of the drag coefficient calculated in the present study with results from other investigators. The first three are from Blanco & Magnaudet (1995) for free-slip conditions, the fourth one is from Magnaudet (personal communication), the last two are from Johnson & Patel (1999) and Magnaudet & Mougin (2007).

3.3. *Grid*

The Lamé curve parameters for the outer boundary are chosen as $n = 4$, $r_1 = z_1 = 80a$. On the basis of standard convergence tests, we settled on a discretization with 81 nodes in the ξ-direction (and, in particular, on the bubble surface) and 61 in the η-direction. The maximum deviation from orthogonality was less than 0.05°, and the minimum radial grid spacing near the bubble surface was less than $0.0091a$. Our resulting grid is almost the same as that used by Blanco & Magnaudet (1995), whose outer boundary was, however, rectangular and therefore introduced singularities in the mapping near the corners. Similar domain sizes were also used in the study of flow past a solid sphere by Natarajan & Acrivos (1993), who had a length of 30 radii downstream of the sphere, Johnson & Patel (1999), who placed the sphere at the centre of a spherical domain with a radius of 30 sphere radii, and Tomboulides & Orszag (2000) and Ghidersa & Dušek (2000), whose downstream length was 50 radii.

3.4. *Validation*

The present grid generation procedure was validated in an earlier paper (Yang *et al.* 2003; see also Yang & Prosperetti 2006). The Navier–Stokes algorithm for the base flow is a simplified form of that developed and validated for a deforming bubble by Yang & Prosperetti (2006).

The problem of the flow past a spheroid with a fixed shape and free-slip conditions has been studied numerically by Dandy & Leal (1986) and Blanco & Magnaudet (1995). The first paper is limited to a maximum Reynolds number of 250 whereas, in the second one, only results up to a maximum aspect ratio of 2.0 are reported.

Table 1 shows a comparison of our computed drag coefficient with the values reported by Blanco & Magnaudet (1995) and others for a free-slip sphere ($\chi = 1.0$) and spheroids, and for a solid sphere. The agreement is satisfactory.

4. Unperturbed flow

We present detailed results for $Re = 660$, which is close to the case discussed by Duineveld (1995). In water, this corresponds to a bubble with an equivalent spherical diameter of about 1.8 mm. The shape of this bubble is closely approximated by a spheroid with semi-axes a and b and an aspect ratio $\chi = b/a = 1.85$. In order to gain an insight into the effect of the deformation, we keep Re fixed at 660 and vary the aspect ratio between 2.0 and 2.5.

The total dimensionless hydrodynamic force, which we refer to, for simplicity, as the drag coefficient, is defined as $C_D = F_D/(\pi b^2 \rho U_\infty^2/2)$, where F_D is the dimensional

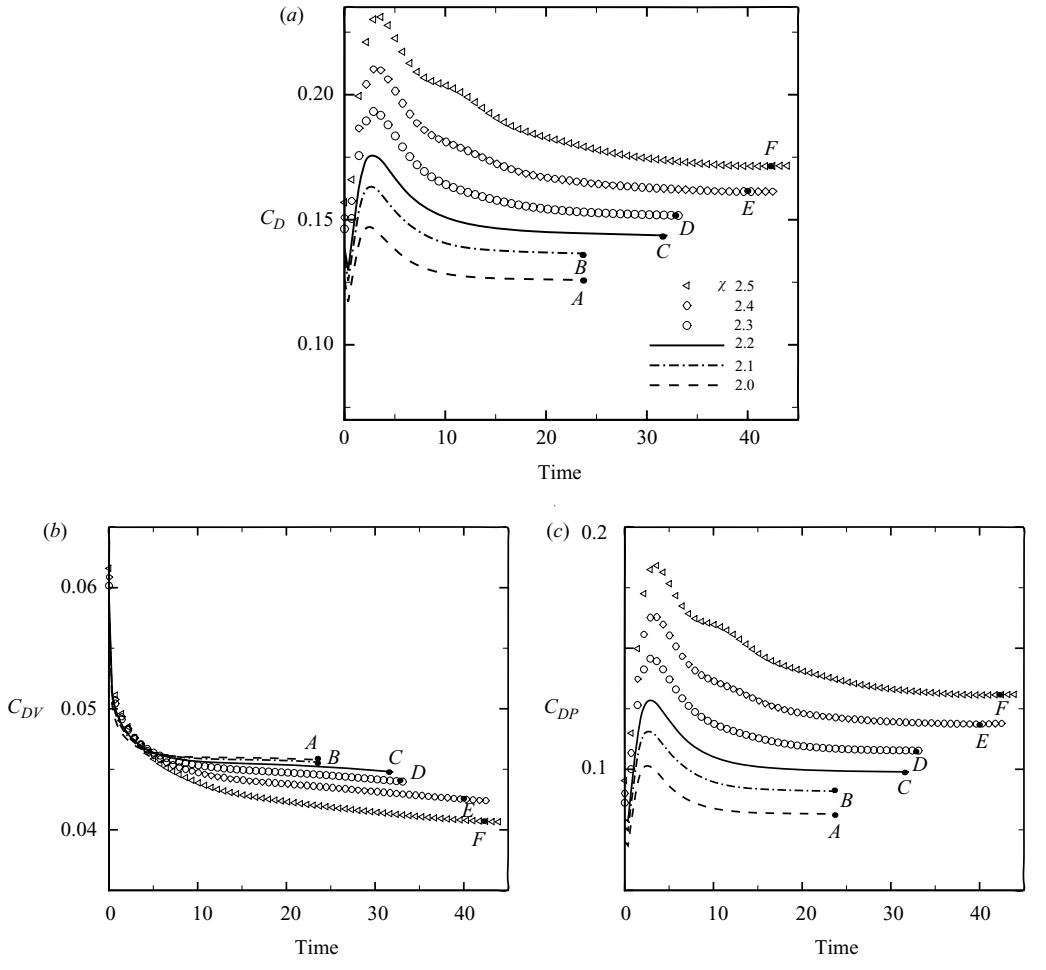

FIGURE 2. Evolution of drag coefficient versus time for axisymmetric flow past a spheroidal bubble of fixed shape for $Re = 660$. The states marked as A, B, C, D, E and F are used as base states for the linear stability calculation. (a) Total drag. (b) Viscous drag. (c) Pressure drag.

hydrodynamic force and ρ the liquid density. This quantity is shown as a function of time in figure 2(a) for different aspect ratios. The pressure, C_{DP}, and viscous, C_{DV}, components of C_D are shown similarly in figures 2(b) and 2(c). The stability analysis reported in the next section will be based on the solutions corresponding to the points marked as A, B, C, D, E and F in these figures.

As the aspect ratio increases, the most significant change in the flow is the increased vorticity generation, proportional to the product of velocity and local curvature, which increases as $\chi^{8/3}$ (Mougin & Magnaudet 2002). Figure 2(a) shows that this circumstance leads to a slower and slower approach to steady state as χ increases.

Figure 3 shows velocity fields and contour plots of vorticity for the states A, B, C, D, E and F of figure 2 corresponding to $\chi = 2.0$, 2.1, 2.2, 2.3, 2.4 and 2.5, respectively. The upper half of each figure shows the velocity field and the lower half contour plots of the vorticity. A standing eddy attached to the rear of the bubble appears in all cases.

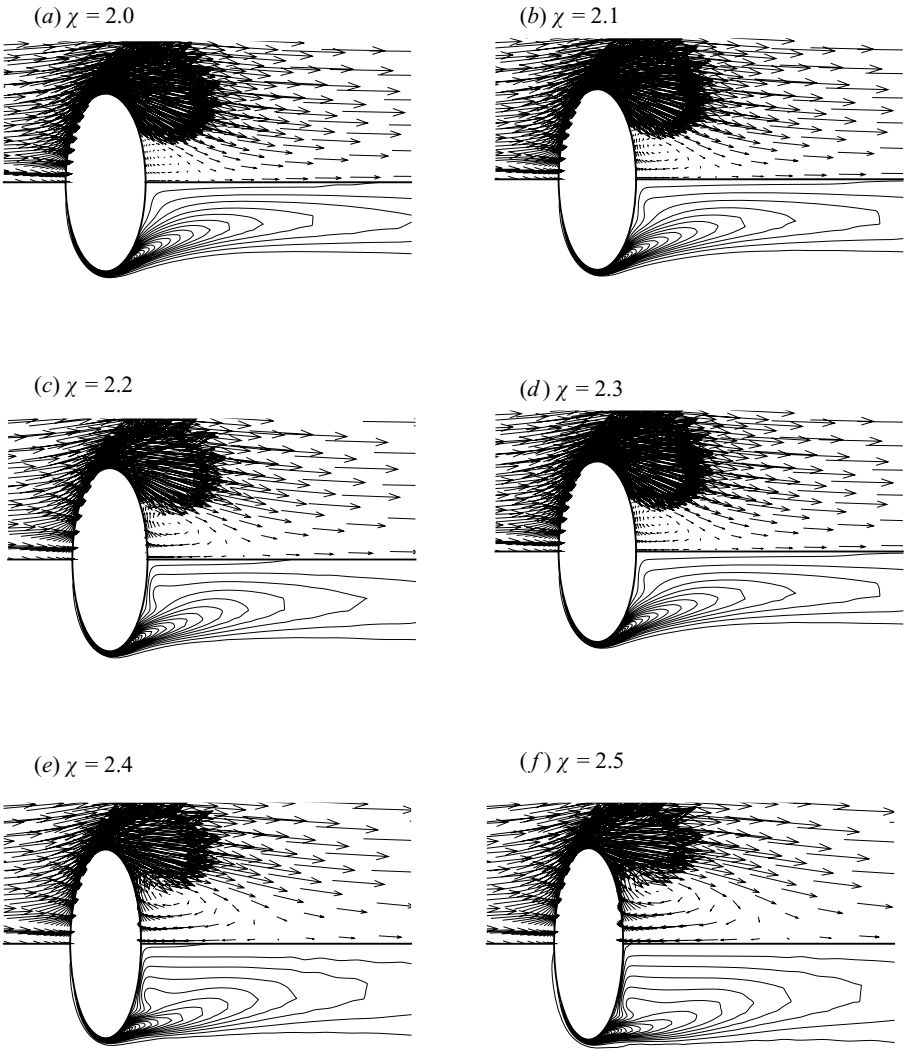

FIGURE 3. Velocity fields (upper half) and vorticity contour plots (lower half) for axisymmetric flow past a spheroidal bubble of fixed shape at Reynolds number $Re = 660$. For each aspect ratio, 50 equally spaced vorticity contours are shown.

Starting the calculation with an already fixed velocity, as we do, leads to a strong vorticity generation during the initial stages. As the flow develops, the boundary layer thickens, the flow separates, and the rate of vorticity generation decreases. The initial vorticity accumulates in the recirculating wake for a while, during which time it develops non-trivial structures with one or more extremal points. Eventually, it diffuses out of the eddy and is convected downstream. This is a slow process during which the total drag coefficient changes little although the viscous contribution to it (figure 2*b*) is still undergoing minor adjustments. On the basis of some tests done at different instants during this late period of adjustment of the flow, we do not expect our conclusions to be significantly affected by this residual slight unsteadiness.

5. Linear stability analysis

In order to characterize the evolution of perturbations we consider the disturbance kinetic energy K

$$K = \frac{1}{2}\sum \left(u_\xi^2 + u_\eta^2 + u_\varphi^2\right), \tag{5.1}$$

where the summation is taken over all the nodes of the computational domain. The amplification factor G of K is defined as

$$G = \frac{K(t^{n+1})}{K(t^n)}. \tag{5.2}$$

For an initial-value problem such as the one we discuss, the perturbation fields will be given by the superposition of eigenmodes with an exponential time dependence (other than in the exceptional case of degenerate eigenvalues). For a regular bifurcation, the leading eigenvalue, λ say, is real and therefore, as time increases,

$$G \to \exp 2\lambda\Delta t \tag{5.3}$$

where $\Delta t = t^{n+1} - t^n$ is the time step. With this relation, λ can be readily determined from the asymptotic value of G. For a Hopf bifurcation, the leading eigenvalue is complex and

$$G \to \exp[2\mathrm{Re}(\lambda)\Delta t]\cos[2\mathrm{Im}(\lambda)\Delta t + \beta], \tag{5.4}$$

where β is a phase. If the leading eigenvalue λ_1 is real and the next one complex, $\lambda_2 = \lambda_2^r + i\lambda_2^i$, the approach to the asymptotic regime (5.3) will be oscillatory:

$$G \simeq \frac{1 + A\exp\left[-2\left(\lambda_1 - \lambda_2^r\right)t^{n+1}\right]\cos\left(\lambda_2^i t^{n+1} + \beta\right)}{1 + A\exp\left[-2\left(\lambda_1 - \lambda_2^r\right)t^{n}\right]\cos\left(\lambda_2^i t^{n} + \beta\right)}\exp(2\lambda_1\Delta t), \tag{5.5}$$

where A is an amplitude and β a phase. The stability features of the system will be evident by analysing the behaviour of K and G.

We studied the stability of the $m = 0$ mode, which probes the steadiness of the base flow. The numerical results show that perturbations either decay for small aspect ratio ($\chi = 2.0$), or exhibit a growth rate very much smaller than that found for the unstable modes. The most unstable mode corresponds to $m = 1$ and these results will be presented first, followed by some results for the mode $m = 2$.

5.1. $m = 1$ *mode*

In considering the results that we now show for the $m = 1$ mode, we should keep in mind that, for this mode, corresponding values of any perturbation quantity on opposite sides of the symmetry axis are negatives of each other.

5.1.1. $m = 1$ *mode – Leading eigenvalue*

Figure 4(*a*) shows the time history of the perturbation kinetic energy K for $\chi = 2.0$, 2.1, 2.2, 2.3, 2.4 and 2.5 at $Re = 660$ associated with the $m = 1$ mode in log–linear coordinates. Figure 4(*b*) shows the corresponding amplification factor G. Clearly K decays for $\chi = 2.0$, whereas it grows very slowly for $\chi = 2.1$ and faster and faster for larger values. The amplification factor G approaches a constant, which indicates a regular bifurcation, and increases with χ. These results show that, for this value of the Reynolds number, the stability threshold in χ is close to 2.1, which is somewhat lower than that of Magnaudet & Mougin (2007) who estimate the threshold at $\chi \simeq 2.2$. We are unable to explain this discrepancy. One possibility is the different nature of the two studies, a linear analysis (ours) *vs.* a nonlinear one. A threshold with $\chi = 2.2$ has

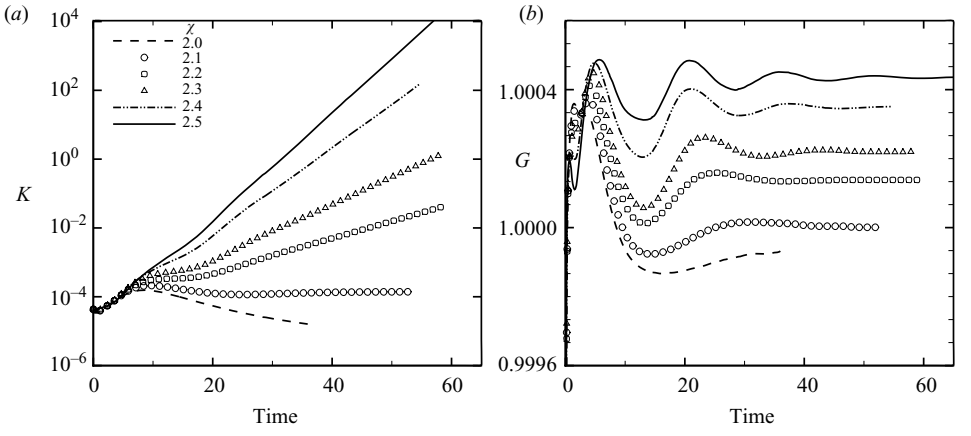

FIGURE 4. Time evolution of (a) the disturbance kinetic energy K in log–linear coordinates and (b) the amplification factor G of the linear stability calculations for $m = 1$ with $Re = 660$.

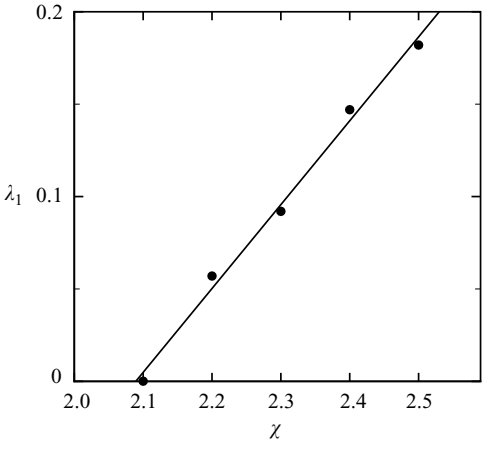

FIGURE 5. The first (real) eigenvalue of the $m = 1$ mode calculated from the amplification factor G at $Re = 660$ as a function of the aspect ratio. The straight line is a linear fit.

also been observed in the experiment of Shew *et al.* (2006), although for $Re = 730$. In any case, this difference does not affect qualitatively our conclusions and, especially, the arguments of § 7.

The eigenvalues for different values of χ can be calculated from the asymptotic values of G according to (5.3) with the result shown in figure 5. The straight line is a least-squares linear fit, $\lambda_1 = 0.454\chi - 0.948$ which crosses 0 for $\chi \simeq 2.09$.

Figure 6 shows the three perturbation vorticity components for $\chi = 2.2$. Figure 6(a) shows the presence of streamwise vorticity localized near the axis. Owing to the proportionality to $\exp(\mathrm{i}\varphi)$, this quantity will have an opposite sign on opposite sides of the axis and will therefore generate a two-threaded wake structure. This axial vorticity becomes significant only at some distance behind the bubble, which would correspondingly delay the appearance of the two-threaded wake as noted by Ghidersa & Dušek (2000) for a solid sphere. Figure 6(b) shows isovorticity lines nearly parallel to the axis downstream of the bubble with a smooth radial variation from negative to positive and then to zero. Inside the recirculating region near the bubble, however,

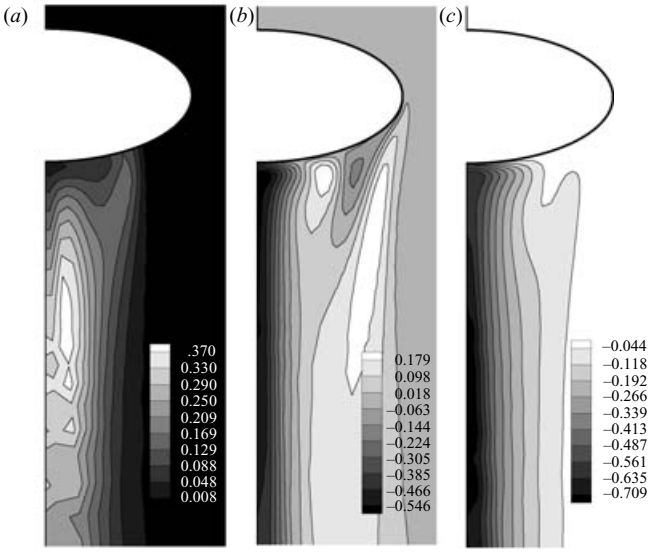

FIGURE 6. Contour plots of the disturbance vorticity components (*a*) ω_z, (*b*) ω_φ and (*c*) ω_r for $\chi = 2.2$ and $Re = 660$ for the $m = 1$ mode.

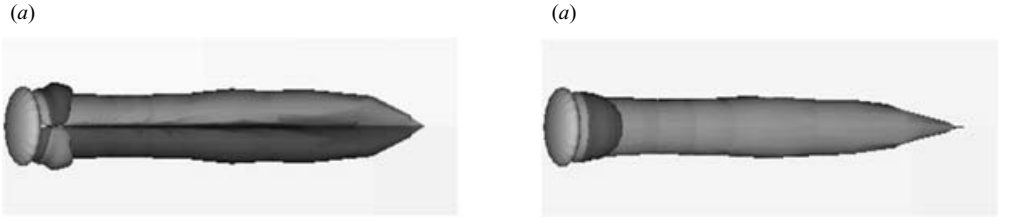

FIGURE 7. Isosurfaces of the streamwise vorticity $\omega_z/\omega_{max} = \pm 0.001$ for the $m = 1$ mode with $Re = 660$, $\chi = 2.3$; ω_{max} is the maximum modulus of the streamwise vorticity. The two views differ by 90°.

two vortex structures with opposite signs form. Again owing to the proportionality to $\exp(i\varphi)$, very near the axis the vorticity is decreased on the right-hand side (shown in the figure, with a minimum value −0.546), but correspondingly enhanced on the left-hand side; as noted before, this feature may be regarded approximately as a translation of the symmetric wake of the base flow.

A view of a typical two-threaded wake (for $\chi = 2.3$) is shown in figure 7 in terms of streamwise iso-vorticity surfaces. The two views differ by 90°, with dark and light shading representing values of streamwise vorticity with the same magnitude but opposite sign. Qualitatively similar results are found for all the other unstable values of χ. The wake depicted here has the characteristic structure found in experiment (Brücker 1999; de Vries *et al.* 2002) and calculation (Mougin & Magnaudet 2002) for bubbles as well as solid spheres (Johnson & Patel 1999; Tomboulides & Orszag 2000). The vector sum of the vorticity components in the φ- and z-directions provides a tilt of the vortex lines as remarked by Thompson *et al.* (2001) for a solid sphere. The small regions with a vorticity of the opposite sign near the bubble are also present in the case of a solid sphere (Tomboulides & Orszag 2000).

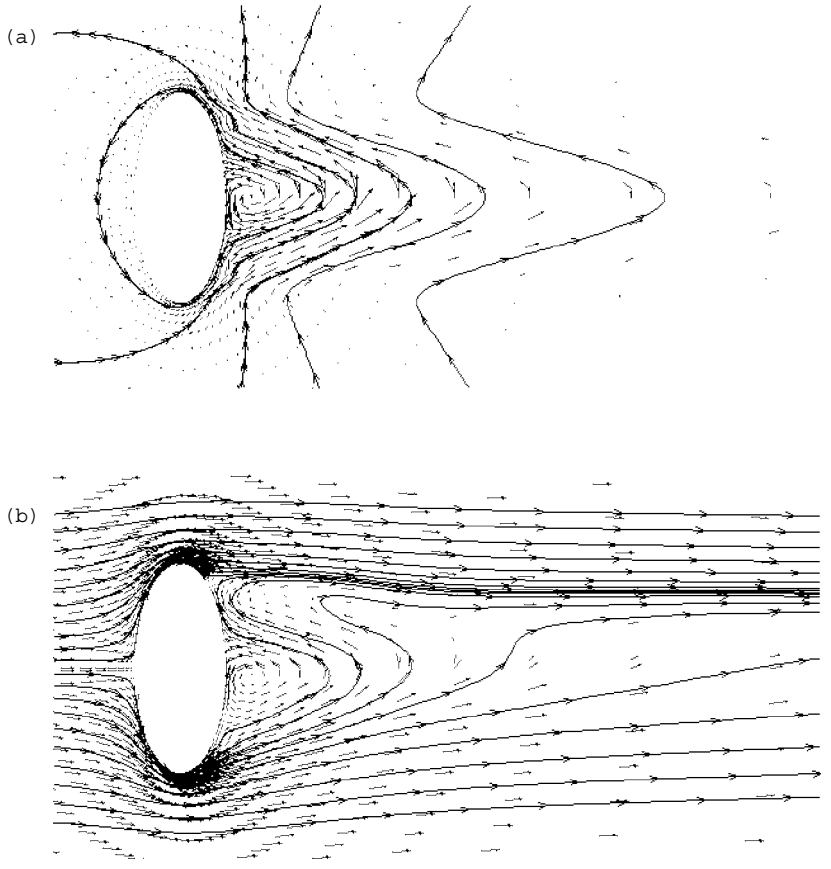

FIGURE 8. Streamlines and velocity vector field for the mode $m = 1$ with $Re = 660$, $\chi = 2.3$ as seen from $\varphi = -\pi/2$; (*a*) perturbation, (*b*) total flow formed by adding 50% of the perturbation to the base flow.

Figure 8(*a*) shows the perturbation streamlines and velocity vector field in the half-planes $\varphi = 0$ and $\varphi = \pi$, whereas figure 8(*b*) gives an impression of the streamlines and velocity field for the total flow obtained by adding to the base flow 50% of the perturbation fields. The flow structure in figure 8(*b*) is similar to that found by Johnson & Patel (1999) in their fully three-dimensional nonlinear simulation of the flow past a fixed solid sphere after the first bifurcation. This conclusion agrees with the point made by Ghidersa & Dušek (2000) in connection with the flow past a solid sphere, where the $m = 1$ mode seems sufficient to capture the essence of the flow. The figure also shows evidence of the spiralling motion of fluid particles on a roughly toroidal trajectory normal to the incident flow shown in figure 12 of Johnson & Patel.

The surface streamlines of the perturbation and of the total flow as observed from the $\varphi = 0$ direction are shown in figures 9(*a*) and 9(*b*), respectively, in two views from 60° above (left) and 60° below (right) the equatorial plane of the bubble. The streamlines of the perturbed flow are formed by arbitrarily adding 25% of the perturbation to the base flow. On the lower side, the perturbation streamlines come together at the roots of the streamwise vortices shown in figure 7, which is also evident in the lower view of the total flow.

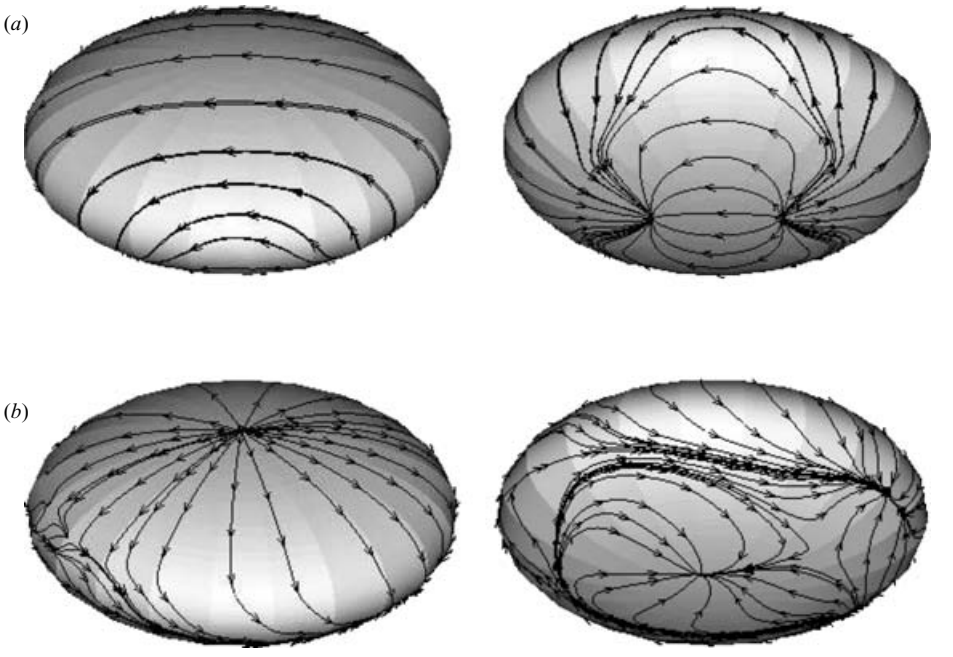

FIGURE 9. Surface streamlines for the mode $m=1$ with $Re=660$, $\chi=2.3$ observed from the $\varphi=0$ direction from 60° above (left) and 60° below (right) the bubble; (*a*) perturbation (*b*) total formed by adding 25% of the perturbation to the base flow.

Figure 10 shows the perturbation surface vorticity components in the angular direction (ω_φ), in the direction normal to the surface (ω_n), and in a tangential direction along the 'meridians' (ω_τ) as they appear along the line $\varphi=\pi/2$. The perturbation vorticity is very small from the front stagnation point to the separation line, as may be expected from the stretching of the vortex lines in this region. When flow convergence accelerates downstream of the separation line, ω_φ rapidly grows in magnitude, followed by ω_n and ω_τ. The angular component of this disturbance vorticity has a strong extremum in the vicinity of the maximum vorticity of the base flow, which indicates a tendency to tilt this 'belt' of maximum vorticity.

Figure 11 shows contour plots of the radial u_r, streamwise u_z, and azimuthal u_φ velocity perturbations associated with the $m=1$ mode for $\chi=2.3$. These results are similar to those for the linearized disturbance flow past a solid sphere given in Natarajan & Acrivos (1993) and, for the fully nonlinear problem, in Tomboulides & Orszag (2000).

5.1.2. *$m=1$ mode – second eigenvalue*

The oscillations of the amplification factors G in figure 4(*b*) before saturation indicate that the second eigenvalue is complex. As the aspect ratio χ is increased, one would expect this eigenvalue to cross the imaginary axis. A similar behaviour is encountered in the case of a solid sphere as the Reynolds number is increased (Natarajan & Acrivos 1993; Johnson & Patel 1999; Tomboulides & Orszag 2000).

Following Tomboulides & Orszag (2000), in order to calculate this second eigenvalue we focus on the time evolution of u_φ (which vanishes at $t=0$) at an arbitrary point behind the bubble. By fitting a function of the form $A(\exp(\lambda_1 t)-1)$ to the large-time numerical results, we find an estimate of the amplitude A of the dominant mode.

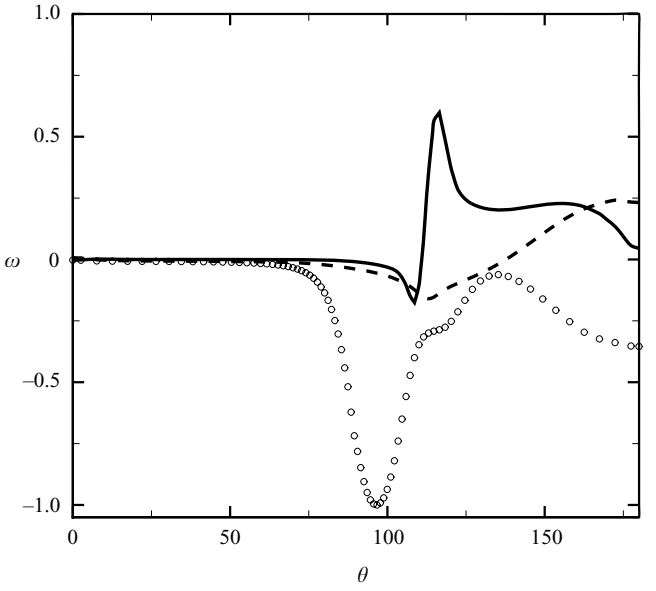

FIGURE 10. Disturbance vorticity components ---, ω_τ; —, ω_n; ○, ω_φ at the bubble surface for the $m=1$ mode with $Re=660$, $\chi=2.3$; θ is the angle measured from the front stagnation point. ω_τ and ω_φ are the tangential components, and ω_n is the normal component. Quantities are normalized by the maximum of $|\omega_\varphi|$.

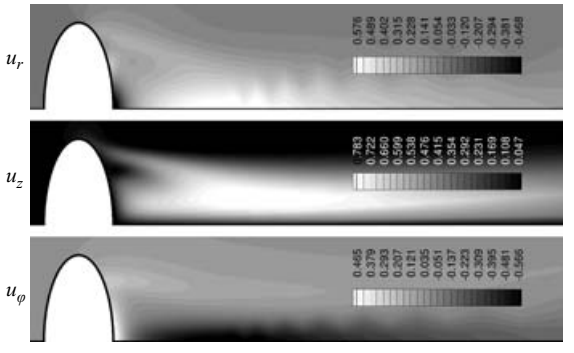

FIGURE 11. Contour plots of the disturbance velocities u_r, u_z, u_φ for $\chi=2.3$ and $Re=660$ for the $m=1$ mode. Ten equally spaced contours are drawn.

The term $A(\exp(\lambda_1 t)-1)$ is then subtracted from $u_\varphi(t)$ and the remainder fitted by an exponential multiplied by a sinusoidal function. In this way, the real and imaginary parts of the second eigenvalue λ_2 can be calculated. The accuracy of this procedure is demonstrated for the case $\chi=2.5$ in figure 12(a) which clearly shows the coexistence of the first, regular, and the second, Hopf, eigenmodes. The second eigenvalue calculated in this way is shown in the complex plane in figure 12(b) for different values of χ.

The eigenfunctions for the second oscillatory mode can also be extracted after subtraction of the leading mode. In figure 13, a series of contour plots of the streamwise λ_2 perturbation vorticity is shown at five different instants of time between $t=30$ and $t=44.4$ covering approximately one period of oscillations, approximately equal to 15.

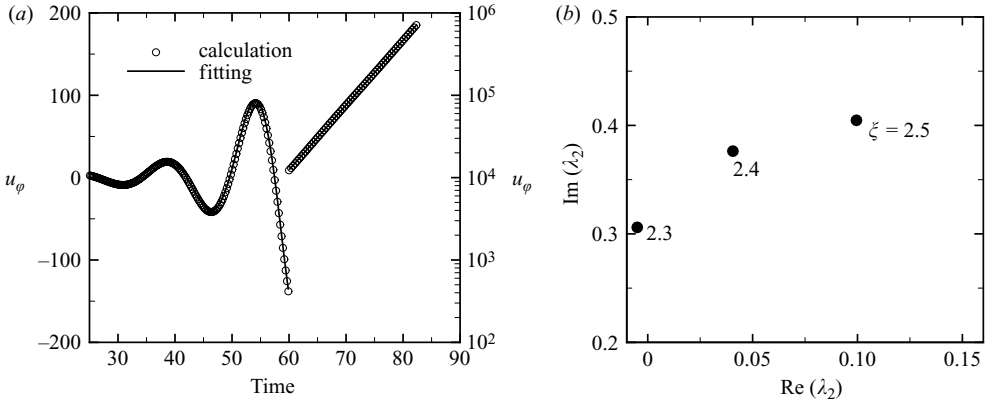

FIGURE 12. (*a*) Illustration of the least-squares fitting procedure to estimate the second eigenvalue. The quantity shown is u_φ at $r \approx 1.5$ and $z \approx -1.8$ for $Re = 660$ and $\chi = 2.5$. The straight lines represent a fit of the leading mode of the form $A(\exp(\lambda_1 t) - 1)$. The oscillating curves show the fit for the second mode after subtraction of the first mode by a function of the form $B \exp[\mathrm{Re}(\lambda_2)t] \cos[\mathrm{Im}(\lambda_2)t + \beta]$. (*b*) Eigenvalues of the second mode obtained by this procedure.

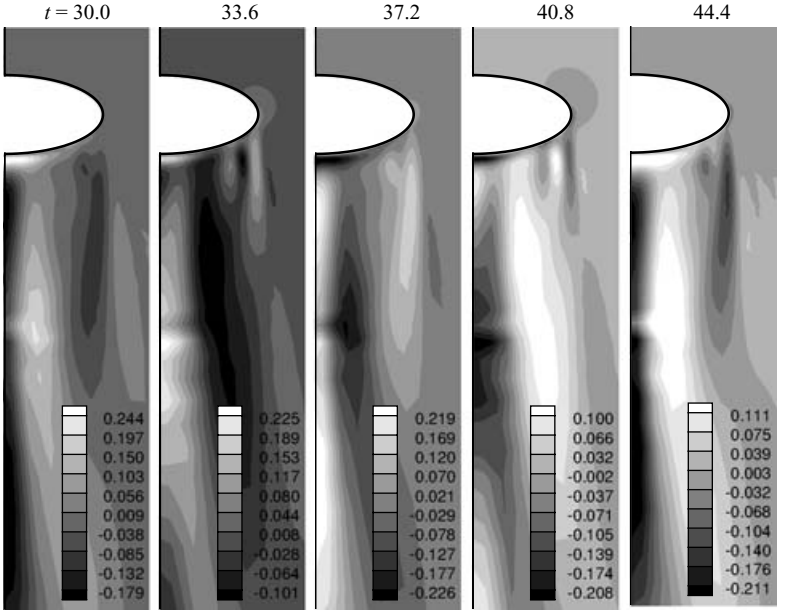

FIGURE 13. A sequence of contour plots of the disturbance vorticity ω_φ in approximately one period for the second (oscillatory) mode of $m = 1$ at $Re = 660$ and $\chi = 2.3$. In each frame, the normalization is according to the maximum magnitude of the perturbation vorticity.

A view of the perturbation vorticity eigenfunction at $t = 44.4$, similar to that of figure 7, is given in figure 14 where the isosurfaces of the streamwise vorticity $\omega_z/\omega_{max} = \pm 0.001$ (with ω_{max} the maximum value) are plotted. By considering the sum of the eigenfunctions corresponding to λ_2 and its complex conjugate, it is found that the sign of the vorticity perturbation would oscillate with the frequency $\mathrm{Im}\,\lambda_2/2\pi$ maintaining a plane of symmetry. This wake structure is similar to that in figure 14

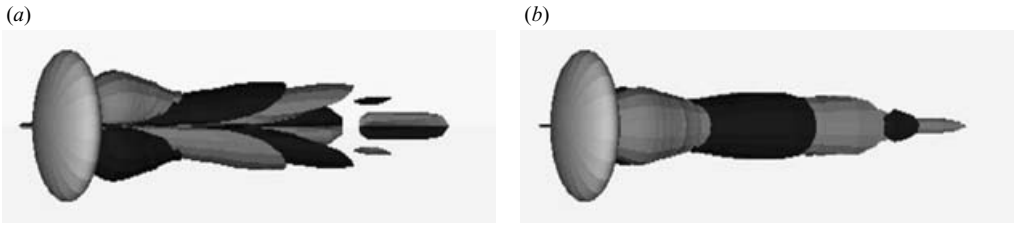

FIGURE 14. Two orthogonal views of the isosurfaces of the streamwise vorticity $\omega_z/\omega_{max} = \pm 0.001$ (with ω_{max} the maximum modulus) for $Re = 660$ and $\chi = 2.3$ for the second eigenfunction of $m = 1$.

χ	Re	λ_1	$\mathrm{Re}(\lambda_2)$	$\mathrm{Im}(\lambda_2)$
2.0	660	<0		
2.1	660	≈ 0.0001	<0	
2.2	330	0.0485	<0	
2.2	660	0.0571	<0	
2.3	200	0.0694	<0	
2.3	330	0.0859	<0	
2.3	400	0.0972	<0	
2.3	660	0.0920	≈ -0.005	0.306
2.4	660	0.147	0.0406	0.376
2.5	150	<0	<0	0.304
2.5	175	0.0271	-0.0139	0.336
2.5	200	0.0625	0.0181	0.342
2.5	330	0.152	0.0771	0.398
2.5	660	0.182	0.0995	0.405

TABLE 2. The first two eigenvalues of the $m = 1$ mode for different Reynolds numbers Re and aspect ratios χ.

of Brücker (1999) for the wake of a solid sphere and is related to the formation and periodic shedding of opposite-signed hairpin vortices (Johnson & Patel 1999; Tomboulides & Orszag 2000).

5.1.3. *Exploring Re–χ parameter space*

Table 2 summarizes the first two eigenvalues for the $m = 1$ mode at different Reynolds numbers and aspect ratios. It is evident that stability is a sensitive function of the aspect ratio, whereas it depends relatively weakly on the Reynolds number. For the same Re, λ_1 increases with increasing aspect ratio while, for fixed χ, the behaviour is more complex as, in some cases (e.g. passing from $Re = 400$ to 660 for $\chi = 2.3$), it decreases with increasing Re. This behaviour is in keeping with the results of figure 7 of Magnaudet & Mougin (2007) which indicates that, for this value of χ, the instability growth rate has a maximum around $Re = 500$. Blanco & Magnaudet (1995) suggested that this result follows from the non-monotonic behaviour with Re of the size of the attached recirculating eddy behind the bubble.

It may be recalled that, for a disk ($\chi \to \infty$) and a solid sphere ($\chi = 1$), the first bifurcation sets in for $Re = 116.5$ and 210, respectively. Our results for a $\chi = 2.5$ spheroidal bubble indicate the onset of the first instability between $Re = 150$ and 175. For the same $\chi = 2.5$, Magnaudet & Mougin (2007) find a slightly higher threshold below about $Re = 180$. Also note that, for different Reynolds numbers, $\mathrm{Im}\,\lambda_2$ takes on similar values close to the second instability onset. The corresponding Strouhal

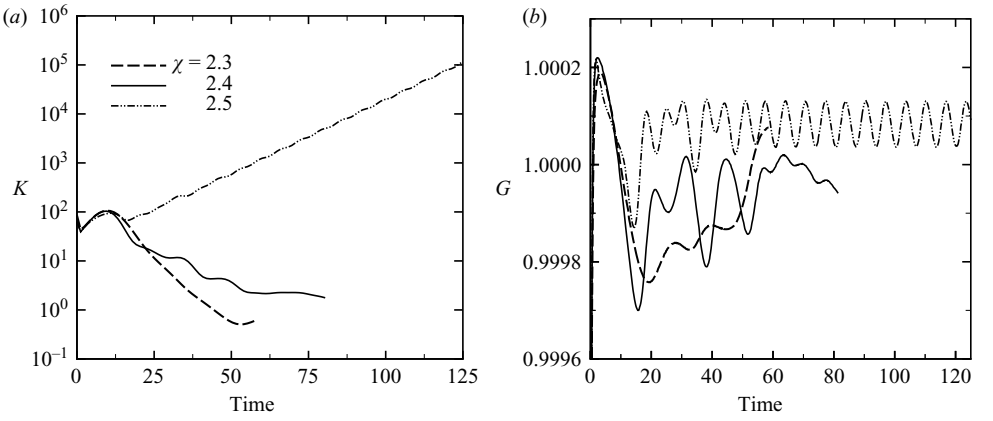

FIGURE 15. Time evolution of (a) the disturbance kinetic energy K in log–linear coordinates and (b) the amplification factor G for $m = 2$ with $Re = 660$.

numbers, $St = 2(\mathrm{Im}\,\lambda_2)/(2\pi)$ are close to 0.1. According to Natarajan & Acrivos (1993), for a solid sphere at onset, $St = 0.113$. For $\chi = 2.5$ and $Re = 330$, our Strouhal number is about 0.13, close to the value found by Magnaudet & Mougin (2007). Our result for $Re = 660$ is somewhat lower than theirs. On the other hand, it is known (see e.g. Pier & Huerre 2001) that linear and nonlinear Strouhal numbers can be rather different, and nonlinear effects may be expected to be much stronger farther away from the threshold.

These values of the Strouhal number are generally consistent with those observed (Mougin & Magnaudet 2002; Shew *et al.* 2006) although the extent to which results for a fixed bubble are applicable to a moving bubble is unclear.

5.2. $m = 2$ mode

Figure 15(a) shows the time history of the disturbance kinetic energy in log–linear coordinates for $\chi = 2.3$, 2.4 and 2.5 at $Re = 660$ for the $m = 2$ mode, and figure 15(b) shows the corresponding amplification factors. K grows exponentially for $\chi = 2.5$ whereas it decays for the smaller values of χ. The oscillatory time dependence of G for $\chi = 2.5$ indicates that the eigenmode is oscillatory, corresponding to a Hopf bifurcation.

The time trace of u_φ at $r \approx 1.5$ and $z \approx -1.8$ is shown in figure 16. Clearly u_φ oscillates, with the oscillation amplitude decaying for $\chi = 2.3$ and 2.4, and growing for $\chi = 2.5$. To separate the real and imaginary parts of the eigenvalue, we assume a functional form $D\exp[\mathrm{Re}(\lambda^{(2)})t]\cos[\mathrm{Im}(\lambda^{(2)})t + \beta]$, where D and β are local constants. As figure 17(a) shows, a good fit can be obtained in this way. The eigenvalue for $\chi = 2.5$ is estimated to be $\lambda^{(2)} \simeq 0.0349 + \mathrm{i}0.476$, while that for $\chi = 2.4$ is estimated to be $\lambda^{(2)} \simeq -0.0430 + \mathrm{i}0.396$.

Two views of the $\omega_z/\omega_{max} = \pm 0.001$ streamwise vorticity isosurfaces rotated by 45° from each other are shown in figure 18 at $t = 54.0$. Other than for the larger number of 'leaves' in the angular direction (4 in place of 2), the structure is similar to that encountered before for the second eigenvalue of the $m = 1$ mode.

6. 'Frozen-state' linear stability calculation

In order to demonstrate the role of the wake development on the instability studied in this paper, it is useful to carry out a 'frozen-state' stability analysis. Here, instead

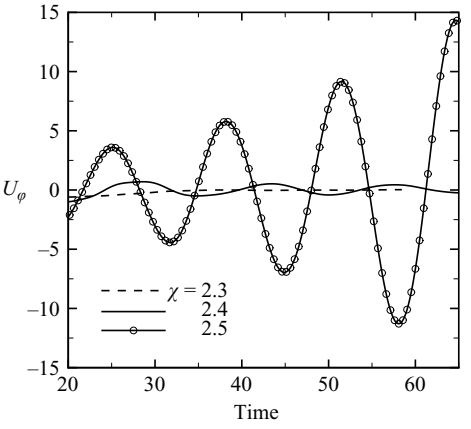

FIGURE 16. Time evolution of u_φ at $r \simeq 1.5$ and $z \simeq -1.8$ for $m = 2$ and $Re = 660$.

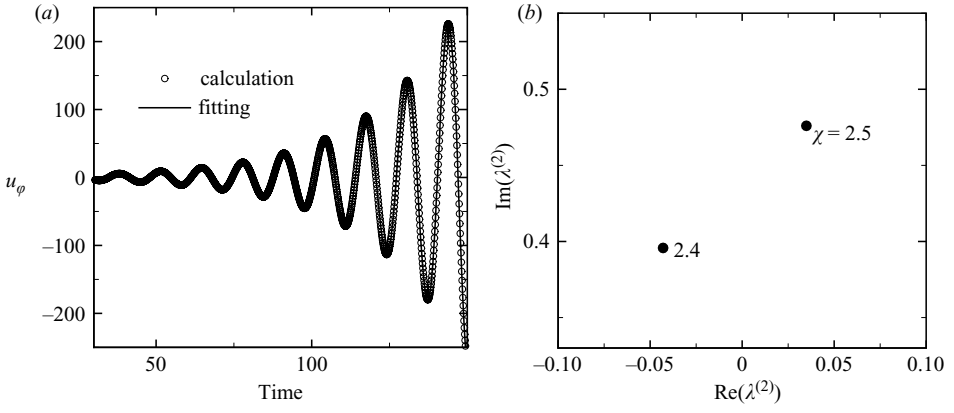

FIGURE 17. (*a*) An example of the least-squares fitting for u_φ at $r \approx 1.5$ and $z \simeq -1.8$ with $Re = 660$ and $\chi = 2.5$ for $m = 2$ according to $D \exp[\mathrm{Re}(\lambda^{(2)})t] \cos[\mathrm{Im}(\lambda^{(2)})t + \beta]$. (*b*) The real and imaginary part of the first eigenvalue for the $m = 2$ mode at $Re = 660$.

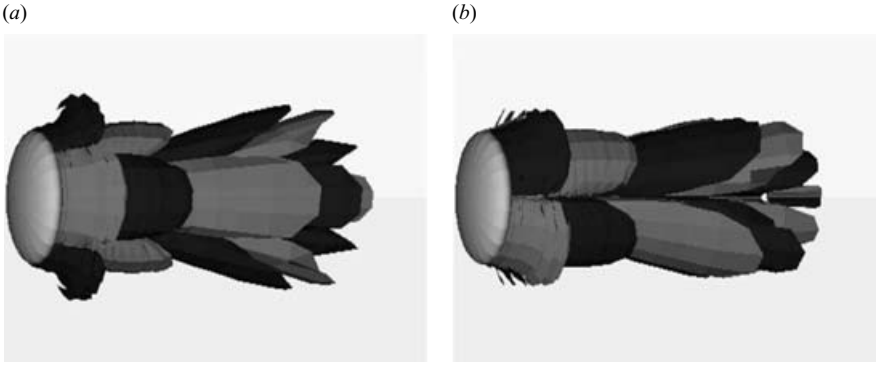

FIGURE 18. Two views rotated by 45° of the isosurfaces of the streamwise vorticity $\omega_z/\omega_{max} = \pm 0.001$ (with ω_{max} the maximum modulus) for $Re = 660$ and $\chi = 2.5$ for the leading eigenvalue of the $m = 2$ mode.

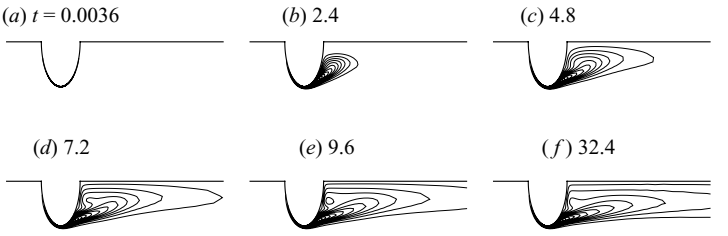

FIGURE 19. Contour plots of vorticity for the axisymmetric flows past a spheroidal bubble of fixed shape at different times with $Re = 660$ and $\chi = 2.3$. At each instant, 40 equally spaced vorticity contours are shown.

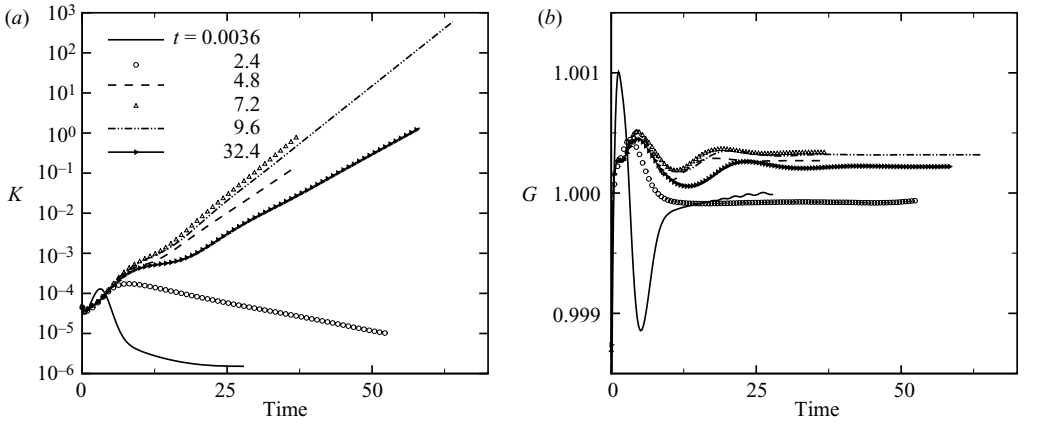

FIGURE 20. Time evolution of (*a*) the disturbance kinetic energy K in log–linear coordinates and (*b*) the amplification factor G of the linear 'frozen' state stability calculations for $m = 1$ with $Re = 660$ and $\chi = 2.3$.

of the steady base flow, we study the stability of 'frozen' snapshots of the evolving unperturbed flow. This procedure is clearly heuristic, but can be justified, first, by noting that the $m = 0$ mode (which would evidently be unstable until the steady state is reached) is separated out in our linearized procedure and, secondly, that for a regular bifurcation, the shape of the unstable eigenfunctions does not change with time so that it would develop in a relatively short time interval during which the still evolving base flow changes little.

We choose the case $Re = 660$ and $\chi = 2.3$ for this analysis. Figure 19 shows a series of contour plots of the base flow vorticity at times $t = 0.0036$, 2.4, 4.8, 7.2, 9.6 and 32.4. The last image corresponds to the point D in figure 2 and is the essentially steady base flow studied before. These contour plots show the evolution of the vortical region behind the bubble which increases with time until generation and convection/dissipation balance.

Figure 20(*a*) shows the time evolution of the disturbance kinetic energy K for the $m = 1$ mode in correspondence with these 'frozen' states, and figure 20(*b*) shows the corresponding amplification factors G. Initially, for $t = 0.0036$ and 2.4, K decays and G remains less than 1, corresponding to a stable situation. For $t \geqslant 4.8$, both quantities show the onset of a regular non-oscillatory instability. The growth rate of the perturbations increases with time between 4.8 and 7.2, but is smaller at 9.2 and even smaller at steady state $t = 32.4$.

We believe that this non-monotonic variation of the growth rate is a consequence of the fact, already noted at the end of §4, that our starting conditions inject a large amount of vorticity into the attached eddy. As long as this vorticity is still in the near wake, it contributes to the destabilization of the flow, which explains the gradual decrease of the instability growth rate as steady conditions are approached. That the flow is still stable at early times, even though this large amount of vorticity is presumably already present in the wake, suggests that the wake volume must be large enough for the instability to set in.

7. Discussion

In their study of the flow past a solid sphere, Johnson & Patel (1999) state that 'the instability of the axisymmetric flow is connected to the generation by radial acceleration around the vortex centre of a ring of low pressure in the wake' (p. 36). Below $Re = 200$, 'the centrifugal force of the vortex rotation must be balanced by viscous forces as opposed to a radial pressure gradient' (p. 28). By simulating the flow past a solid no-slip sphere, we have confirmed the appearance of these local pressure minima at $Re = 200$, i.e. below the first bifurcation at $Re = 210$. We found the same structures in the simulation of free-slip spheroids where, at $Re = 660$, a clear pressure minimum already occurs for $\chi = 2.0$ and, in general, well below the instability threshold also for other Reynolds numbers. Thus, the occurrence of a pressure minimum may well be a factor but, by itself, it appears to be insufficient to account for the instability.

Magnaudet & Mougin (2007) analayse the equation for the base-flow vorticity ω_ϕ which, in our notation, is

$$U_r \frac{\partial \Omega_\phi}{\partial r} - U_r \frac{\Omega_\phi}{r} + U_z \frac{\partial \Omega_\phi}{\partial z} = \nu \left[\frac{\partial}{\partial r} \left(\frac{1}{r} \frac{\partial (r \Omega_\phi)}{\partial r} \right) + \frac{\partial^2 \Omega_\phi}{\partial z^2} \right]. \tag{7.1}$$

They argue that, as the aspect ratio increases, there is a region near the rear of the bubble in which the iso-Ω_ϕ lines gradually tilt normally to the z-axis until a portion of them nearly coincides with constant z-lines. In this region, $\partial \Omega_\phi / \partial r \simeq 0$ and the equation is satisfied by an approximate balance of $(U_z \partial \Omega_\phi / \partial z - U_r \Omega_\phi / r)$ and $\nu \partial^2 \Omega_\phi / \partial z^2$, which requires a stronger and stronger vorticity variation in the streamwise direction as the Reynolds number is increased. On this basis, they hypothesize that a sufficient criterion for the onset of the instability is the appearance of a line (or a region) where $\partial \Omega_\phi / \partial r = 0$. 'Existence of this region is specific to axisymmetric flows and results from the combination of the Prandtl–Batchelor constraint within the standing eddy and the condition of weak vorticity on the rear part of the body surface' (Magnaudet 2006). The argument developed by Magnaudet is compelling, although it does not quite explain the actual mechanism of the instability.

Vortex rings are known to be subject to a variety of instabilities (see e.g. Widnall & Sullivan 1973; Tsai & Widnall 1976; Maxworthy 1977; Saffman 1978; Dritschel 1988; Kopiev & Chernyshev 1997). This possibility is mentioned, among others, by Thompson *et al.* (2001) in their study of sphere wake transition. Via the Biot-Savart induced velocity field, a rearrangement of the vorticity in the wake would perturb the ambient flow in which the bubble finds itself immersed. A consequence of this disturbance of the flow incident on the bubble would be a spatial redistribution of the vorticity generation, which could be such as to reinforce the perturbation. In order for this to happen, it is not even necessary that the vorticity distribution become unstable

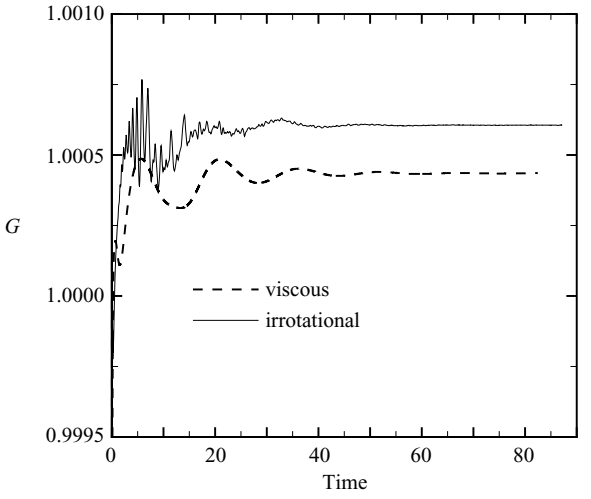

FIGURE 21. Growth rate of a quasi-irrotational perturbation (see text) with $m = 1$ (solid line) compared with that of the regular vortical one for $\chi = 2.5$ and $Re = 660$.

itself. One of the various oscillation modes that can be supported by vortices (see e.g. Kopiev & Chernyshev 1997) would be sufficient to disturb the axial symmetry.

A trigger for a process of this type could be the surface vorticity shown in figure 10. The convergence of the undisturbed streamlines as the flow approaches the rear stagnation point of the bubble has the effect of amplifying any disturbance affecting the vorticity of the base flow. This disturbed vorticity, which acts as a boundary condition for the disturbance vorticity equation, would have a strong effect on the vorticity distribution behind the sphere and might destabilize it.

In the hope of gaining some further understanding of the phenomenon, we have carried out some stability simulations trying to minimize the perturbation vorticity by setting the viscosity to zero and replacing the free-slip condition on the bubble surface by a condition of irrotationality. Unfortunately, this procedure does not completely eliminate the perturbation vorticity as the term $(\boldsymbol{\omega}\cdot\nabla)\boldsymbol{u}$ in the vorticity equation will act as a source of perturbation vorticity. We found that the (properly scaled) magnitude of the perturbation vorticity in the region of the base flow attached vortex is comparable in the two calculations. A result of this analysis, however, is that the growth rate of the instability is increased with respect to the viscous case (see figure 21 for an example). This feature is characteristic of instabilities rooted in inertial effects.

As for the second mode $m = 1$ bifurcation, its oscillatory nature points to a standard shear-flow instability encountered, for example, in the analysis of the stability of the flow past a cylinder in two dimensions (Yang & Zebib 1989).

8. Conclusions

In order to shed light on the origin of the path instability of a rising gas bubble in a liquid, we have studied the linear stability of the axisymmetric flow past a fixed spheroid with free-slip boundary conditions and different aspect ratios χ and Reynolds numbers Re. The first instability corresponds to the mode $m = 1$. For a fixed moderate Reynolds number, a gradual increase of χ causes first a regular bifurcation to a steady flow with a fixed plane of symmetry and a double-threaded wake, followed by a second Hopf bifurcation. A similar sequence is found for a fixed

χ and increasing Re (table 2). At larger Reynolds numbers or aspect ratios, the mode $m = 2$ also becomes unstable.

According to the experiments of Duineveld (1995), an air bubble rising in hyperclean water starts zigzagging at an equivalent radius of 0.91 mm, with an aspect ratio of about 1.85 and a Reynolds number of 662. Our result for the threshold at this Reynolds number is approximately $\chi = 2.1$ which, according to Duineveld's figure 3, would correspond to an equivalent radius of 0.99 mm. Because a real gas bubble does not quite have a spheroidal shape, rises freely rather than being constrained as in our simulation, and might exhibit shape oscillations, the agreement appears to be satisfactory.

The first bifurcation to a steady plane-symmetric flow, with its two-threaded wake, can explain the appearance of a lift force perpendicular to the original axis of symmetry. The Hopf bifurcation that takes place with a larger χ or Reynolds number modulates the lift force produced by the first bifurcation. The bifurcation sequence in the present axisymmetric flow is therefore qualitatively different from that of two-dimensional flows in that transition to unsteady flow is not the result of the first bifurcation.

Qualitatively, our results resemble those found for the flow past a solid sphere in spite of the different boundary conditions on the body surface, whose effect appears essentially to move the instability onset to larger Reynolds numbers. As pointed out by Leal (1989), this feature is probably related to the different strength of vorticity generation at the bubble surface. The role of vorticity is highlighted by our stability study of the base flow 'frozen' at different instants before becoming steady. We have found that, initially and for some time after the start of the simulation, the flow is stable. Only when enough vorticity has accumulated in the wake and has reached a suitable spatial distribution, these 'frozen states' start becoming unstable.

By setting viscosity to zero in the perturbation equations, we finds that the growth rate of the primary instability increases, which suggests that the instability is rooted in inertial effects.

A. P. is pleased to acknowledge many fruitful discussions with A. Biesheuvel, D. Lohse, J. Magnaudet and L. van Wijngaarden. The comments of J. Magnaudet have been especially valuable. Thanks are also due to D. G. Dritschel, W. L. Shew, and C. Veldhuis.

This study has been supported by NASA under grant NNC05GA47G.

REFERENCES

Achenbach, E. 1974 Vortex shedding from spheres. *J. Fluid Mech.* **62**, 209–221.

Aybers, N. M. & Tapucu, A. 1969*a* The motion of gas bubbles rising through stagnant liquid. *Wärme und Stoffübertragung* **2**, 118–128.

Aybers, N. M. & Tapucu, A. 1969*b* Studies on the drag and shape of gas bubbles rising through a stagnant liquid. *Wärme und Stoffübertragung* **2**, 171–177.

Batchelor, G. 1967 *An Introduction to Fluid Mechanics*. Cambridge University Press.

Benjamin, T. 1987 Hamiltonian theory for motions of bubbles in an infinite liquid. *J. Fluid Mech.* **181**, 349–379.

Blanco, A. & Magnaudet, J. 1995 The structure of axisymmetric high-Reynolds number flow around an ellipsoidal bubble of fixed shape. *Phys. Fluids* **7**, 1265–1274.

Brown, D. L., Cortez, R. & Minion, M. L. 2001 Accurate projection methods for the incompressible Navier–Stokes equations. *J. Comput. Phys.* **168**, 464–499.

Brücker, C. 1999 Structure and dynamics of the wake of bubbles and its relevance to bubble interaction. *Phys. Fluids* **11**, 1781–1796.

Clift, R., Grace, J. & Weber, M. 1978 *Bubbles, Drops, and Particles*. Academic.

Dandy, D. S. & Leal, L. G. 1986 Boundary layer separation from a smooth slip surface. *Phys. Fluids* **29**, 1360–1366.

Dritschel, D. G. 1988 Nonlinear stability bounds for inviscid, two-dimensional, parallel or circular flows with monotonic vorticity, and the analogous three-dimensional quasi-geostrophic flows. *J. Fluid Mech.* **191**, 575–581.

Duineveld, P. 1995 The rise velocity and shape of bubbles in pure water at high Reynolds number. *J. Fluid Mech.* **292**, 325–332.

Duraiswami, R. & Prosperetti, A. 1992 Orthogonal mapping in two dimensions. *J. Comput. Phys.* **98**, 254–268.

Ellingsen, K. & Risso, F. 2001 On the rise of an ellipsoidal bubble in water: oscillatory paths and liquid-induced velocity. *J. Fluid Mech.* **440**, 235–268.

Ghidersa, B. & Dušek, J. 2000 Breaking of axisymmetry and onset of unsteadiness in the wake of a sphere. *J. Fluid Mech.* **423**, 33–69.

Goldburg, A. & Florsheim, B. H. 1966 Transition and Strouhal number for the incompressible wake of various bodies. *Phys. Fluids* **9**, 45–50.

Hartunian, R. & Sears, W. 1957 On the stability of small gas bubbles moving uniformly in various liquids. *J. Fluid Mech.* **3**, 27–47.

Jenny, M., Dušek, J. & Bouchet, G. 2004 Instabilities and transition of a sphere falling or ascending freely in a Newtonian fluid. *J. Fluid Mech.* **508**, 201–239.

Johnson, T. & Patel, V. 1999 Flow past a sphere up to a Reynolds number of 300. *J. Fluid Mech.* **378**, 19–70.

Kopiev, V. F. & Chernyshev, S. A. 1997 Vortex ring eigen-oscillations as a source of sound. *J. Fluid Mech.* **341**, 19–57.

Leal, L. G. 1989 Velocity transport and wake structure for bluff bodies at finite Reynolds number. *Phys. Fludis* A **1**, 124–131.

Lunde, K. & Perkins, R. J. 1997 Observations on wakes behind spheroidal bubbles and particles. In *ASME Fluids Engineering Division Summer Meeting*, paper 3530.

Lunde, K. & Perkins, R. 1998 Shape oscillations of rising bubbles. *Appl. Sci. Res.* **58**, 387–408.

Magarvey, R. H. & Bishop, R. L. 1961 Transition ranges for 3-dimensional wakes. *Can. J. Phys.* **39**, 1418–1422.

Magnaudet, J. 2006 A physical mechanism for the primary instability of axisymmetric wakes past bluff bodies. *Bull. Am. Phys. Soc.* **51** (9), 128–129.

Magnaudet, J. & Eames, I. 2000 The motion of high-Reynolds-number bubbles in inhomogeneous flows. *Annu. Rev. Fluid Mech.* **32**, 659–708.

Magnaudet, J. & Mougin, G. 2007 Wake instability of a fixed spheroidal bubble. *J. Fluid Mech.* **572**, 311–338.

Magnaudet, J., Rivero, M. & Fabre, J. 1995 Accelerated flow past a rigid sphere or a spherical bubble. Part 1. Steady straining flow. *J. Fluid Mech.* **284**, 97–135.

Maxworthy, T. 1977 Some experimental studies of vortex rings. *J. Fluid Mech.* **81**, 465–495.

Meiron, D. 1989 On the stability of gas bubbles rising in an inviscid fluid. *J. Fluid Mech.* **198**, 101–114.

Moore, D. 1965 The velocity of rise of distorted gas bubbles in a liquid of small viscosity. *J. Fluid Mech.* **23**, 749–766.

Mougin, G. & Magnaudet, J. 2002 Path instability of a rising bubble. *Phys. Rev. Lett* **88**, 014502/1.

Natarajan, R. & Acrivos, A. 1993 The instability of the steady flow past spheres and disks. *J. Fluid Mech.* **254**, 323–344.

Ormières, D. & Provansal, M. 1999 Transition to turbulence in the wake of a sphere. *Phys. Rev. Lett*. **83**, 80–83.

Pier, B. & Huerre, P. 2001 Nonlinear self-sustained structures and fronts in spatially developing wake flows. *J. Fluid Mech.* **435**, 145–174.

Prosperetti, A. 2004 Bubbles. *Phys. Fluids* **16**, 1852–1865.

Ryskin, G. & Leal, L. 1983 Orthogonal mapping in two dimensions. *J. Comput. Phys.* **98**, 254–268.

Ryskin, G. & Leal, L. 1984 Numerical solution of free-boundary problems in fluid mechanics. Part 2. Buoyancy-driven motion of a gas bubble through a quiescent liquid. *J. Fluid Mech.* **148**, 19–35.

Saffman, P. G. 1956 On the rise of small air bubbles in water. *J. Fluid Mech.* **1**, 249–275.

Saffman, P. G. 1978 The number of waves on unstable vortex rings. *J. Fluid Mech.* **84**, 625–639.

el Sawi, M. 1974 Distorted gas bubbles at large Reynolds number. *J. Fluid Mech.* **62**, 163–183.

Schouveiler, L. & Provansal, M. 2002 Self-sustained oscillations in the wake of a sphere. *Phys. Fluids* **14**, 3846–3854.

Shew, W. L., Poncet, S. & Pinton, J.-F. 2006 Force measurements on rising bubbles. *J. Fluid Mech.* **569**, 51–60.

Takagi, S., Matsumoto, Y. & Huang, H. 1997 Numerical analysis of a single rising bubble using boundary-fitted coordinate system. *JSME Intl J.* B **40**, 42–50.

Thompson, M. C., Leweke, T. & Provansal, M. 2001 Kinematics and dynamics of sphere wake transition. *J. Fluids Struct.* **15**, 575–585.

Tomboulides, A. G. & Orszag, S. A. 2000 Numerical investigation of transitional and weak turbulent flow past a sphere. *J. Fluid Mech.* **416**, 45–73.

Tsai, C.-Y. & Widnall, S. E. 1976 The stability of short waves on a straight vortex filament in a weakly externally imposed shear. *J. Fluid Mech.* **73**, 721–733.

Veldhuis, C., Biesheuvel, A., van Wijngaarden, L. & Lohse, D. 2005 Motion and wake structure of spherical particles. *Nonlinearity* **18**, C1–C8.

de Vries, A., Biesheuvel, A. & van Wijngarden, L. 2002 Notes on the path and wake of a gas bubble rising in pure water. *Intl J. Multiphase Flow* **28**, 1823–1835.

Widnall, S. E. & Sullivan, J. P. 1973 On the stability of vortex rings. *Proc. R. Soc. Lond.* A **332**, 335–353.

Yang, B. & Prosperetti, A. 2006 A second-order boundary-fitted projection method for free-surface flow computations. *J. Comput. Phys.* **213**, 574–590.

Yang, B., Prosperetti, A. & Takagi, S. 2003 The transient rise of a bubble subject to shape or volume changes. *Phys. Fluids* **15**, 2640–2648.

Yang, X. & Zebib, A. 1989 Absolute and convective instability of a cylinder wake. *Phys. Fluids* A **1**, 689–696.